

# Robust unsupervised 5D seismic data reconstruction on regular and irregular grids

Ji Li<sup>1</sup>, Dawei Liu<sup>2</sup>, Daniel Trad<sup>1</sup>, and Mauricio D. Sacchi<sup>2</sup>

## ABSTRACT

Seismic data reconstruction has become a central focus in seismic data processing, addressing challenges posed by sparse sampling due to physical and budgetary constraints. The advent of 5D acquisition methodologies marks a significant advancement in the quality and completeness of seismic data sets. Most traditional 5D reconstruction methods commonly use the fast Fourier transform (FFT), requiring regular grids and preliminary 4D binning before 5D interpolation. Discrete Fourier transform and nonequidistant FFT can honor the original irregular coordinates. However, when using exact locations, these methods become computationally expensive. We introduce an unsupervised deep-learning methodology to learn a continuous function across the sampling points in seismic data, facilitating reconstruction on

regular and irregular grids. The network comprises a multilayer perceptron with linear layers and element-wise periodic activation functions. It excels at mapping the input coordinates to the corresponding seismic data amplitudes without relying on external training sets. The network's intrinsic low-frequency bias is crucial in prioritizing acquiring self-similar features over high-frequency and incoherent ones during training. This characteristic mitigates incoherent noise in seismic data, such as random and erratic components. To assess the robustness of the unsupervised reconstruction technique, we conduct comprehensive evaluations using synthetic data examples sampled regularly and irregularly, as well as field-data examples with and without binning. The findings demonstrate the efficacy of our deep-learning framework in achieving resilient and accurate seismic data reconstruction across diverse sampling scenarios.

## INTRODUCTION

Due to physical and budgetary constraints, seismic data are often irregularly sampled along spatial coordinates, requiring a multidimensional reconstruction process during processing. Over the past two decades, various practical algorithms have been proposed to address this challenge.

Prediction error filters, as introduced by Spitz (1991), Porsani (1999), and Naghizadeh and Sacchi (2009), offer a method to interpolate aliased seismic traces. In addition, transform-based methods, notably the Fourier transform (Sacchi and Ulrych, 1995, 1996; Sacchi et al., 1998; Zwartjes and Gisolf, 2007; Li et al., 2012; Chiu, 2014; Mosher et al., 2017), are widely used in the industry, particularly in 5D seismic data reconstruction (Liu and Sacchi, 2004; Trad, 2009; Jin, 2010). Other predetermined transforms such as the Radon transform (Bardan, 1987; Kabir and Verschuur, 1995; Wang et al., 2010), wavelet transform (Wang and Li, 1994), and curvelet

transform (Herrmann and Hennenfent, 2008; Hennenfent et al., 2010) can also be used for interpolating missing traces. Dictionary learning has been introduced and shows promise in 5D reconstruction (Wang et al., 2021) to enhance the adaptability of the transform to the data being processed.

Another category of traditional approaches is based on rank reduction theory, assuming that complete data are low-rank, with missing traces and noise leading to higher rank (Ely et al., 2013). Rank reduction methods operate on matrices (Trickett et al., 2010; Oropeza and Sacchi, 2011; Gao et al., 2013a; Kumar et al., 2015; Sternfels et al., 2015; Chen et al., 2016) and tensors (Kreimer and Sacchi, 2012; Kreimer et al., 2013; Ely et al., 2015; Gao et al., 2015, 2016; Carozzi and Sacchi, 2019; Popa et al., 2021; Cavalcante and Porsani, 2022; Liu et al., 2022). The final category within traditional approaches encompasses wave-front-attribute-based methods (Baykulov and Gajewski, 2009; Hoecht et al., 2009; Xie and Gajewski, 2016, 2017). These methods are data-driven and leverage

Manuscript received by the Editor 9 February 2024; revised manuscript received 26 June 2024; published ahead of production 14 July 2024.

<sup>1</sup>University of Calgary, Department of Earth, Energy and Environment, Calgary, Alberta, Canada. E-mail: li.ji1@ucalgary.ca; daniel.trad@ucalgary.ca.

<sup>2</sup>University of Alberta, Department of Physics, Edmonton, Alberta, Canada. E-mail: 409791715@qq.com (corresponding author); msacchi@ualberta.ca.

© 2024 Society of Exploration Geophysicists. All rights reserved.

information from physical quantities, such as the angle of emergence and wave-front attributes, rather than relying solely on mathematical transforms.

In recent years, deep-learning algorithms have emerged as a promising avenue for seismic data interpolation. These algorithms fall into two categories: supervised (Oliveira et al., 2018; Wang et al., 2019; Qian et al., 2021) and unsupervised (Park et al., 2020; Yuan et al., 2021). Although supervised methods require extensive external training data sets, unsupervised methods eliminate this need but demand more computational time. Based on conventional neural networks, both categories are restricted to 2D or 3D data reconstruction due to the computational costs associated with high-dimensional networks.

A significant limitation shared by traditional reconstruction methods using the Fourier transform, specifically the fast Fourier transform (FFT), and deep-learning methods using convolutional neural networks (CNNs) is their reliance on seismic data deployed on regular grids. Given the irregular sampling of seismic data along spatial dimensions, a prerequisite for reconstruction is binning data into regularly sampled spatial dimensions. This process typically involves storing and representing data as regular matrices or tensors, a step in which the transition from the off-the-grid to the on-the-grid data will inevitably introduce artifacts. Moreover, the bin size becomes an additional parameter that must balance computational complexity with precision. Notably, this binning process can compromise the continuity of the seismic wavefield, leading to a loss of fidelity in the reconstructed data. Addressing this issue is crucial for improving the accuracy and reliability of seismic data reconstruction methods, particularly as we advance toward handling more complex and higher-dimensional data sets.

The discrete Fourier transform (Duijndam et al., 1999; Xu et al., 2005) has been applied to develop reconstruction methods that can directly handle irregularly sampled seismic data, enabling a more accurate and faithful representation of the underlying wavefield. Another approach involves using the FFT coupled with intermediate interpolation methods to reconstruct seismic data accurately, preserving the exact spatial locations. Noteworthy methods include non-equispaced FFT (Duijndam and Schonewille, 1999; Keiner et al., 2009; Jin, 2010; López et al., 2016) and extended projection onto convex set (EPOCS) (Jiang et al., 2017). However, these techniques entail significant computational and memory resources, rendering them less practical for handling the complexity of 5D seismic interpolation. In contrast, whether deep learning can enhance interpolation performance by dealing with irregular coordinates remains an intriguing area of exploration.

Recently, implicit neural representation (INR) has emerged as a promising signal processing framework characterized by a multi-layer perceptron (MLP) that incorporates linear layers and element-wise nonlinear activation functions. INR learns a continuous function over a set of points, making it well suited for handling irregularly sampled signals such as high-dimensional seismic data (Liu et al., 2024). Unlike CNNs, INRs are free of locality biases, contributing to enhanced performance. Recent successes of the INR span applications similar to surface representation (Sitzmann et al., 2020), volume rendering (Martin-Brualla et al., 2021; Mildenhall et al., 2021), and generative modeling (Chan et al., 2021). They demonstrate that an INR can be interpreted as a structured signal representation dictionary (Yüce et al., 2022), wherein the nonlinear activation function dictates the atoms of the dictionary. For exam-

ple, the sine activation creates a pseudo-Fourier transform representation of the seismic signal that is sparsely concentrated across several frequency spectra (Yüce et al., 2022).

This paper proposes a robust, unsupervised framework consisting of an MLP that combines linear layers and an element-wise sinusoidal activation function to reconstruct multidimensional seismic data. The proposed framework can reconstruct regularly binned and unbinned seismic data with original irregular spatial coordinates. In the proposed network, the training input consists of each data point's 5D coordinates (one temporal coordinate and four spatial coordinates). In contrast, the training target is the amplitude at the corresponding coordinate. Specifically, the proposed method learns a continuous mapping from the seismic data's spatial and temporal coordinates to the seismic data's amplitude. Subsequently, the trained model can predict the seismic data at the desired regular coordinates. The proposed method can effectively attenuate random and erratic noise during training when combined with a modified weight initialization function, robust loss function, and early stopping. Synthetic and field data examples demonstrate that the proposed algorithm can reconstruct 5D seismic data on regular and irregular grids.

## THEORY

### Implicit neural representation

The objective of the INR is to encode a continuous target signal  $d$  using a neural network  $f_\theta$ , parameterized by a set of weights  $\theta$ . This network represents the mapping between input coordinates  $\mathbf{c}$  and signal values  $d_c$ . The encoding process involves minimizing a distortion measure, such as the mean-squared error, through the gradient descent during training. The continuous nature of INR proves particularly advantageous when handling irregularly sampled signals.

However, a significant challenge for INRs is effectively reconstructing the high-frequency details in most multimedia signals. INR and classical neural network architectures such as CNNs demonstrate a well-documented spectral bias toward lower frequencies (Rahaman et al., 2019; Xu, 2020; Huh et al., 2021), traditionally limiting their use in implicit representation tasks. Recent efforts have introduced various solutions to mitigate this spectral bias. For example, Tancik et al. (2020) propose incorporating a Fourier mapping layer before the MLP, whereas Sitzmann et al. (2020) suggest using an MLP with sinusoidal activations. Both approaches aim to bias the networks toward higher frequencies. In this study, we adopt a network similar to the one proposed by Sitzmann et al. (2020), using the sinusoidal activation function to synergize with the MLP.

The architecture of the INR with a sinusoidal activation function can be decomposed as follows:

$$f_\theta(\mathbf{c}) = \mathbf{W}^{(L)} \mathbf{z}^{(L-1)} + \mathbf{b}^{(L)}, \quad (1)$$

where

$$\begin{cases} \mathbf{z}^{(0)} = \sin(\omega_0(\mathbf{W}^{(0)}\mathbf{c} + \mathbf{b}^{(0)})) \\ \mathbf{z}^{(\ell)} = \sin(\mathbf{W}^{(\ell)}\mathbf{z}^{(\ell-1)} + \mathbf{b}^{(\ell)}), \quad \ell = 1, \dots, L-1 \end{cases}. \quad (2)$$

Here,  $\mathbf{c}$  denotes the input coordinate to the first layer  $\mathbf{z}^{(0)}$ , which is followed by multiple layers of an MLP, represented as  $\mathbf{z}^{(\ell)}$ . Each layer is characterized by its respective weights  $\mathbf{W}^{(\ell)}$  and biases  $\mathbf{b}^{(\ell)}$ . A sinusoidal activation function is applied element-wise at each layer  $\ell = 0, \dots, L-1$ . The constant  $\omega_0$  is used for parameter

rescaling at the initial stage. A larger  $\omega_0$  biases the network toward higher frequencies, thus mitigating the low-frequency spectral bias observed in traditional neural networks.

## INR for seismic data interpolation

In the context of seismic data, INR performs a mapping from the coordinate systems to the signal value space. For example, in the 2D case, the function is represented as  $f(t, x) = d$ , where  $t$  is the time,  $x$  is the offset, and  $d$  corresponds to the signal value at that specific coordinate. In the 3D case, the equation becomes  $f(t, hx, hy) = d$ , with  $hx$  and  $hy$  representing the two horizontal spatial dimensions. This formulation can extend to a 5D case with different coordinates as well. For instance, supposing that the four spatial dimensions (common midpoint inline/crossline, offset, and azimuth) are denoted as  $mx, my, h$ , and  $az$ , the function becomes  $f(t, mx, my, h, az) = d$ . A simplified illustration of the network architecture is shown in Figure 1. The network itself is straightforward, comprising an input layer representing the coordinates of the seismic data and an output layer corresponding to the response amplitude of the seismic data. At its core, the network features a fully connected MLP augmented with sinusoidal activation functions.

The uniqueness of the INR interpolation method lies in its departure from conventional supervised training methods that depend on extensive external data sets for training, which are often challenging to acquire for real seismic data. INR efficiently achieves data training by parameterizing seismic signals using only a single data set. Furthermore, compared with traditional methods, our INR method can work directly on data sets with irregular sampling grids without binning, avoiding introducing artifacts caused by the binning process.

Figure 2 shows two different sampling methods along the spatial dimension: uniform sampling with regular intervals and random sampling with irregular intervals. In the first case, we use the network to minimize the cost function

$$\min_{\theta} \sum_{i=1}^N \rho(f_{\theta}(\mathbf{c}_1^i) - d_{\mathbf{c}_1^i}), \quad (3)$$

where  $\mathbf{c}_1^i$  represents the coordinate of  $i$ th observed data points, with a total of  $N$  points for training. These coordinates are generated by a sampling operator  $S$  that extracts a subset of the coordinate vectors from the uniform sampling set  $C_1$  by  $SC_1 = \{\mathbf{c}_1^i\}_{i=1}^N$ . The distortion measure  $\rho$  represents a general loss function, such as  $\ell_1$ ,  $\ell_2$ , and the Huber loss. The Huber loss is a piece-wise function that combines elements of the  $\ell_1$  and  $\ell_2$  loss functions. It behaves like the  $\ell_2$  loss for small differences (less than a specified threshold  $\delta$ ) and like the  $\ell_1$  loss for larger differences. Mathematically, the Huber loss is defined as

$$\rho_H(a; \delta) = \begin{cases} \frac{1}{2}a^2 & \text{for } |a| \leq \delta \\ \delta \cdot (|a| - \frac{1}{2}\delta) & \text{otherwise} \end{cases}, \quad (4)$$

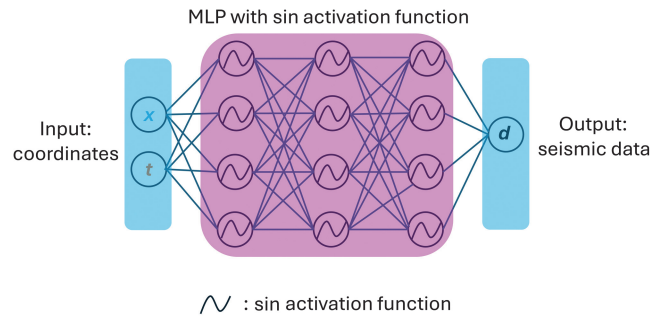


Figure 1. INR interpolation network with MLP and a sin activation function.

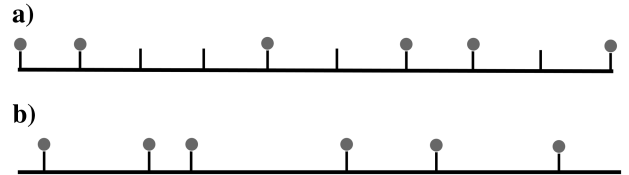


Figure 2. Two sampling methods on a spatial dimension, the gray circle indicates the data point. (a) Uniform sampling with regular intervals and (b) random sampling with irregular intervals.

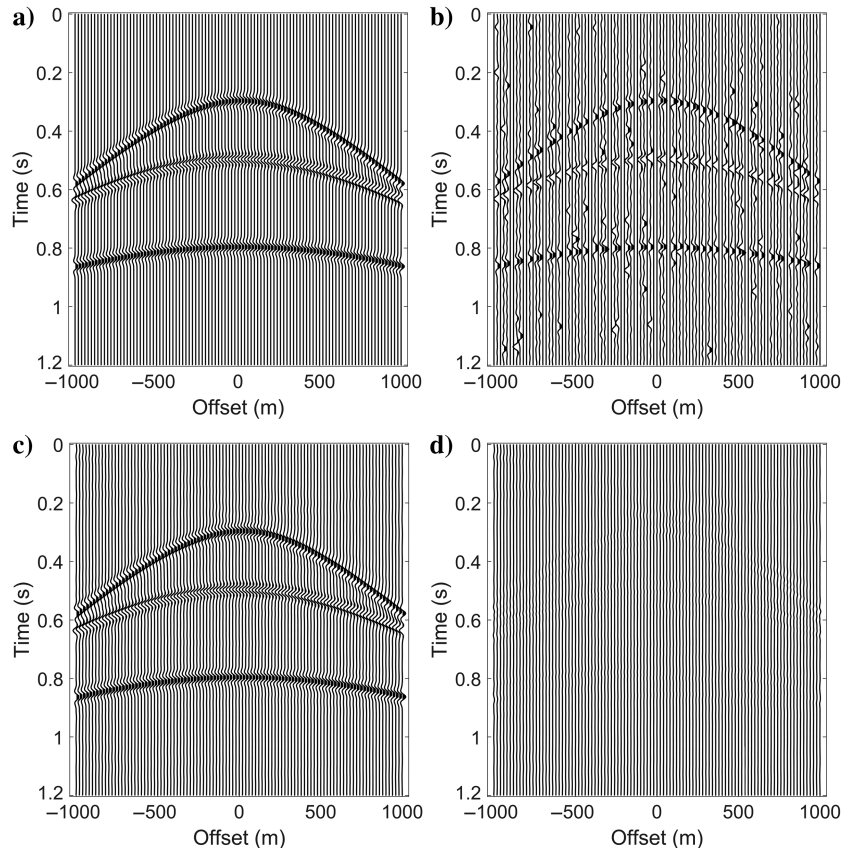


Figure 3. The 2D synthetic example on a regular grid. (a) The original data, (b) noisy decimated data with missing traces, (c) reconstructed result ( $S/N = 17.47$  dB), and (d) errors between (a) and (c).

Figure 4. The 2D synthetic example on an irregular grid. (a) The original data, (b) noisy undersampled data on an irregular grid, (c) reconstructed result on the same regular grid as (a) ( $S/N = 17.51$  dB), and (d) errors between (a and c).

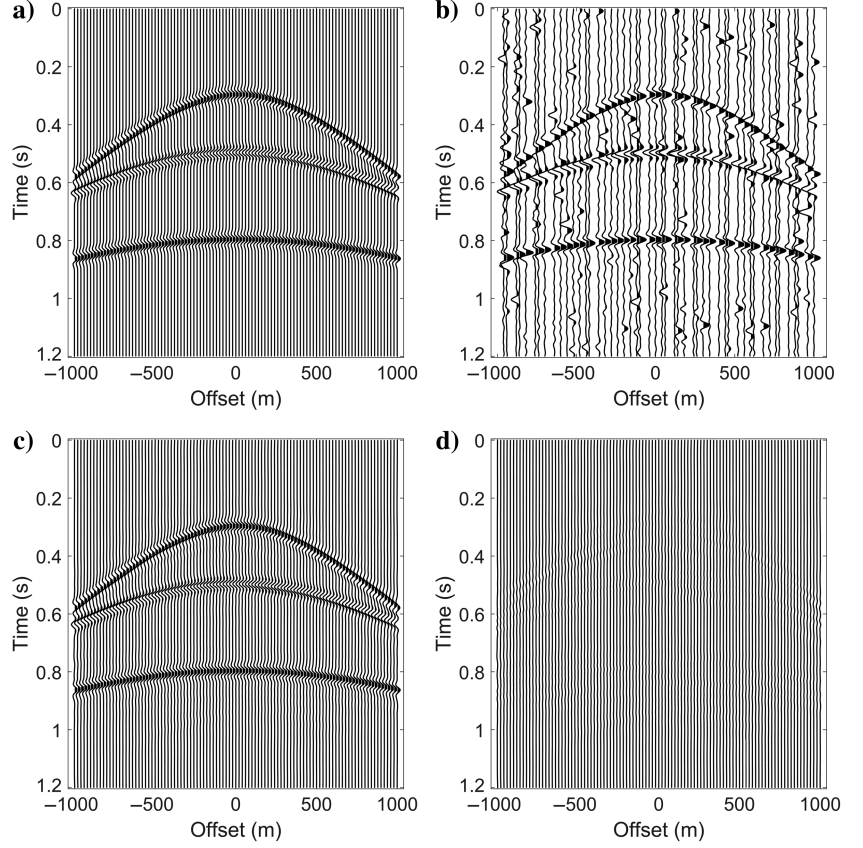
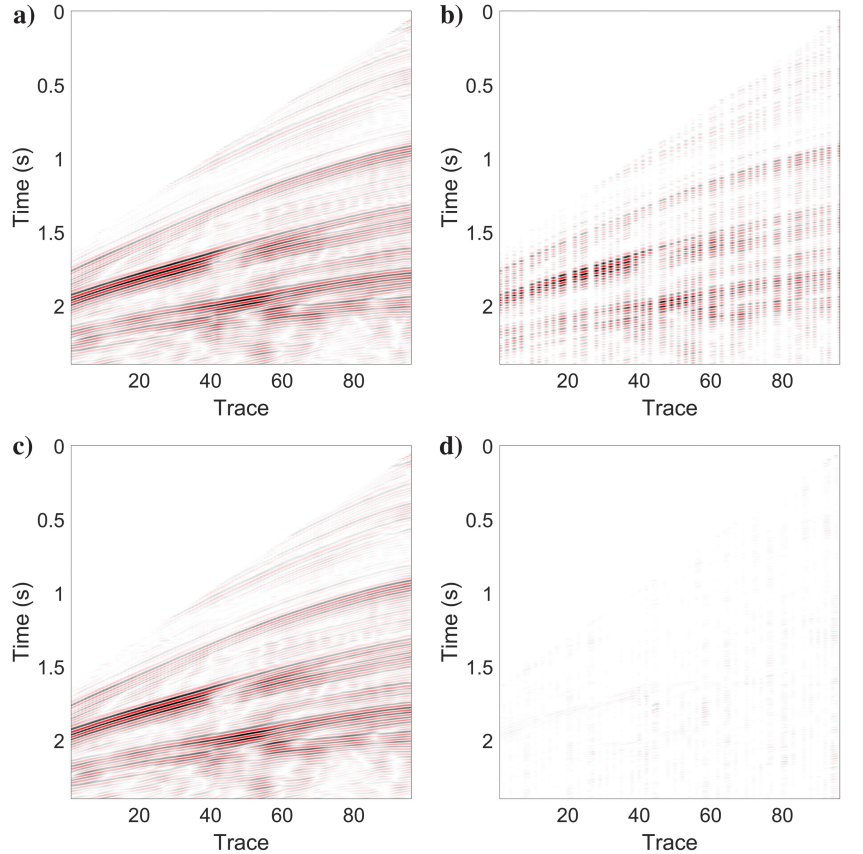


Figure 5. The 2D synthetic example generated from the Marmousi model. (a) The original data, (b) decimated data with 50% of the trace randomly removed, (c) reconstructed result ( $S/N = 20.96$  dB), and (d) errors between (a and c).



where  $a$  is the error term (e.g., the difference between the predicted value and the true value), and  $\delta$  is the threshold that determines the point at which the loss function transitions from quadratic to linear. We use  $\delta = 0.1$  in the Huber loss function in our examples. This loss function is less sensitive to outliers than  $\ell_2$  loss and is often used to reconstruct seismic data contaminated by erratic noise (Carozzi and Sacchi, 2019). After training,  $d_{\mathbf{c}_1} = f_\theta(\mathbf{c}_1)$  represents the final interpolated data at any missing positions.

In the second case, we aim to minimize the loss function

$$\min_{\theta} \sum_{i=1}^N \rho(f_\theta(\mathbf{c}_2^i) - d_{\mathbf{c}_2^i}), \quad (5)$$

where  $\mathbf{c}_2^i \in \mathcal{C}_2$  and  $\mathcal{C}_2$  is the off-the-grid coordinate set in Figure 2b. Unlike the situation with  $\mathcal{C}_1$ , there is no need for a sampling operator  $S$  to ensure  $SC_2 = \{\mathbf{c}_2^i\}_{i=1}^N$  because each point in  $\mathbf{c}_2^i$  directly corresponds to the available data  $d_{\mathbf{c}_2^i}$ . After training, we can produce the seismic data at any desired coordinate, including uniform grids in Figure 2a with  $f_\theta(\mathbf{c}_1)$ .

Yüce et al. (2022) prove that the frequency support of the reconstruction  $f_\theta(\mathbf{c})$  is entirely controlled by the frequency support from the initialization of the first layer. In our case, this is controlled by  $\omega_0$ . Using a small value of  $\omega_0$  will limit the reconstruction by missing many high-frequency features. Higher initialization fundamental frequencies have been proven to lead to faster convergence (Sitzmann et al., 2020; Tancik et al., 2020). However, initializing the frequencies above an appropriate level may produce aliasing artifacts (Barron et al., 2021). Choosing  $\omega_0 = 30$  rad/s, as suggested by Sitzmann et al. (2020), provides a balance, allowing the satisfactory reconstruction of critical features while avoiding aliasing effects. In our case, with incomplete seismic data contaminated with pronounced high-frequency noise, we aim to represent the underlying signals accurately while excluding the noise. This necessitates a trade-off in choosing  $\omega_0$  that should be large enough to represent the signals effectively yet not so large as to incorporate excessive noise. This approach aligns with traditional reconstruction methods based on the Fourier transform with a band-pass filter.

Yüce et al. (2022) also indicate that the multi-layer structure of INRs imposes a particular low-rank structure over the coefficients, similar to the sparsity assumption in classical dictionaries (Tošić and Frossard, 2011). The network tends to suppress the learning of noise in the early stages. Prolonged training risks overfitting to the noise; however, low-rank regularization ensures that the network does not learn the noisy data in their original form. A similar observation is mentioned in Xu and Jiao (2023). Therefore, with a small  $\omega_0$ , a robust loss function, and an early stop, our network not only reconstructs the missing data but also attenuates noise in the data simultaneously. Further exploration into the optimal selection of  $\omega_0$ , choice of a robust loss function, and determination of the ideal early stopping point will be addressed in the Discussion section.

## EXAMPLES

### 2D examples

#### Simple 2D example

We first test a simple 2D synthetic data example, as shown in Figure 3a. We begin by randomly removing half of the traces and then adding some random and erratic noise to the data. Figure 3b shows the resulting noisy data. We then use our proposed method with a regular grid to reconstruct the data, as shown in Figure 3c. Figure 3d shows the differences between the original clean data and the reconstructed result.

To further investigate the adaptability of our method, we extend our evaluation to an irregular grid configuration, as shown in Figure 4b. In this case, instead of reconstructing the missing traces, we leverage the precise coordinates of the traces for network training. The well-trained model is then applied to predict the reconstructed data on the desired regular grid, which is subsequently visualized on the regular grid, mirroring the configuration of Figure 4a. The reconstructed data set is shown in Figure 4c, demonstrating the method's versatility in handling irregularities in the data distribution.

#### Marmousi 2D example

Our method is capable of interpolating complex data as well. We demonstrate its capability with a 2D synthetic data example derived

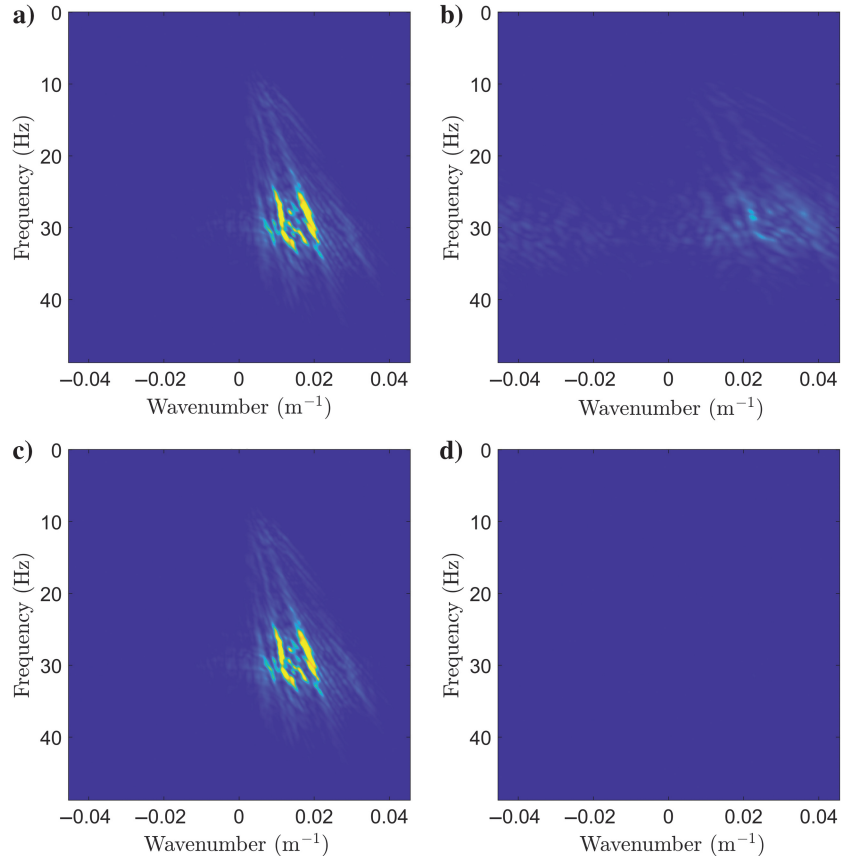


Figure 6. The FK panel of the Marmousi data example. (a) The original data, (b) decimated data with 50% of the trace removed regularly, (c) reconstructed data, and (d) errors between (a) and (c).

from the Marmousi earth model. Figure 5a presents a single-shot gather from the Marmousi data set, whereas Figure 5b shows the same data with 50% of the traces randomly removed. Our method's interpolated result with the irregular coordinates is presented in Figure 5c, along with the associated signal-to-noise ratio (S/N) value. Figure 5d shows the errors between the interpolated results and the original data. Figure 6 shows the corresponding frequency-wavenumber (FK) panel.

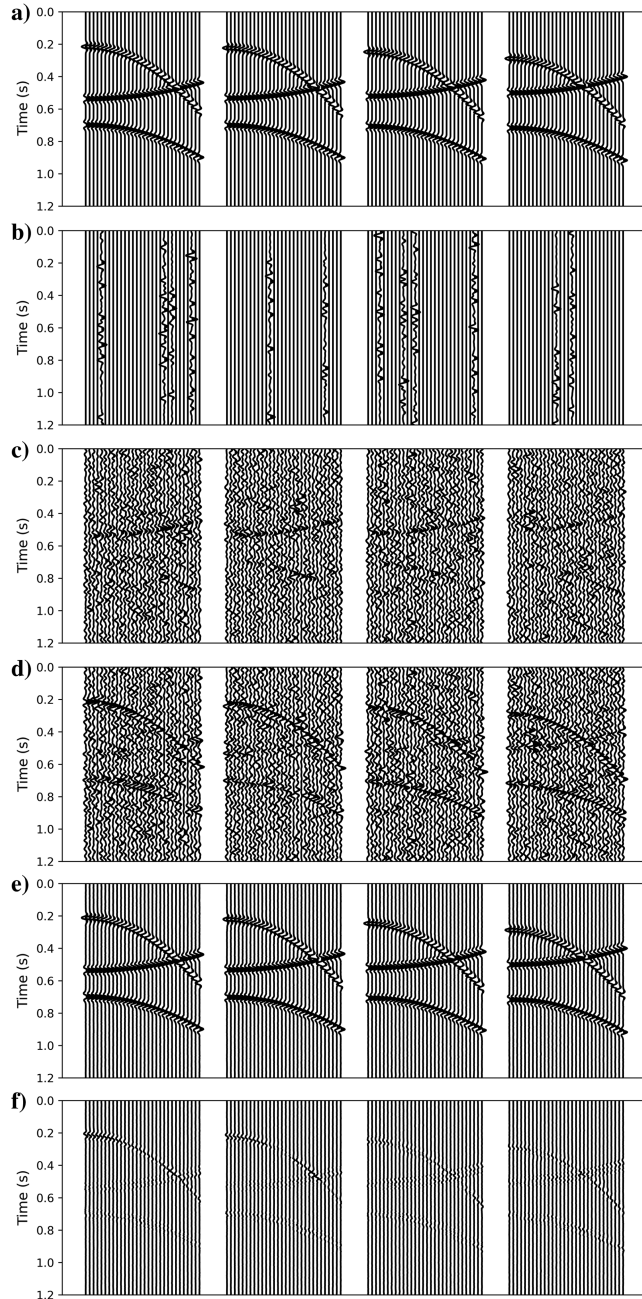


Figure 7. The synthetic 5D example consists of random and erratic noise with missing 90% traces. (a) The original data, (b) decimated data with random and erratic noise, (c) POCS reconstruction ( $S/N = -3.1$  dB), (d) errors between (a and c), (e) robust INR reconstruction ( $S/N = 13.95$  dB), and (f) errors between (a and e).

## 5D examples

In this section, we thoroughly test our robust method with experiments on three types of 5D data sets: synthetic 5D examples on a regular grid, a binned real 5D data example, and an authentic 5D data set with irregular coordinates devoid of binning. To streamline the training process for all 5D data examples, we systematically divide each data set into smaller patches measuring  $64 \times 1$ , ensuring a 50% overlap for comprehensive coverage. Throughout the training phase, we maintain a batch size of 1024. We use the Adam optimizer with a fixed learning rate of  $1e^{-5}$  to ensure stable convergence during optimization. To avoid overfitting, we implement an  $\ell_1$  loss function. For all the 5D examples, we use  $\omega_0 = 10$  rads/s.

In addition to evaluating our proposed method, we conduct a comparative analysis with the widely used conventional 5D reconstruction method, projection onto convex sets (POCS) (Abma and Kabir, 2006; Gao et al., 2013b). We use POCS with a linear threshold schedule for all instances and iterate it 100 times. This comparative assessment aims to provide a meaningful benchmark and insight into the relative performance of our proposed robust method against a well-established approach in the field.

### Synthetic 5D examples on a regular grid

We generate a spatial data volume with the dimensions  $30 \times 30 \times 12 \times 8$ , comprising 301 time samples at a sampling rate of 4 ms. This volume represents the seismic traces, with the first two spatial dimensions denoting the common midpoint  $x$  (CMP $x$ ) and the common midpoint  $y$  (CMP $y$ ). The third and fourth dimensions represent the offset and azimuth, respectively. The volume contains three parabolic events. To simulate realistic conditions, we introduce random and erratic noise to the data and subsequently randomly remove 90% of the traces. The synthetic data are then used to train our proposed network, and the training process concludes after 10 epochs. In Figure 7a, we present the data for azimuth bins 1–4 with fixed offset and CMP $y$ . Figure 7b shows the decimated data with random and erratic noise. The lack of remaining traces presents a significant challenge for successful reconstruction. Figure 7c shows the reconstructed result using the POCS method, a conventional approach for 5D reconstruction. Due to strong noise and the absence of 90% of the traces, POCS failed to reconstruct this data set, resulting in an S/N of  $-3.1$  dB compared with the original data in Figure 7a. Finally, Figure 7e shows the reconstructed result obtained using our robust INR method. Our method surpasses the POCS approach not only in reconstructing continuous events but also in attenuating noise. The S/N of the reconstructed data improved to  $13.95$  dB. This example shows the robust capability of the proposed method in accurately characterizing the continuous seismic wavefield. By comparing costs, we observe that the POCS method required 42 s to reconstruct the data set using MATLAB. In contrast, the proposed robust INR method, executed on a consumer-grade graphics card boasting 7680 CUDA cores and 12 GB of RAM, completes one epoch in 15 s, totaling 2.5 min for data set reconstruction. A direct cost comparison between these two methods is inappropriate because POCS uses CPU, whereas the proposed method uses GPU. However, it still indicates that the cost difference between the two methods is insignificant. More importantly, the proposed method significantly outperforms other deep-learning methods in handling high-dimensional data. For instance,

CNN-based methods typically demand several hours to train one epoch on a 5D data set. Our approach effectively reduces the problem to 1D by training the network on continuous points leveraging the MLP. The input is comprised of points with five features, whereas the output consists of points with just one feature.

#### Binned real 5D example

We continue our evaluation and apply the proposed robust INR method to a binned real 5D data set. This data set features spatial dimensions of  $30 \times 30 \times 7 \times 6$ , incorporating 351 time samples at a 4 ms sampling rate. Experimental settings, as in the previous scenario, are used. The network concludes training after 50 epochs. The consistent parameters alleviate the burdensome process of parameter selection, further demonstrating the robustness of our method. In Figure 8a, we present the data corresponding to azimuth bins 1–4 with a fixed offset and CMPy. These gathers are selected to compare performance across large gaps. The reconstructed results achieved by the POCS and robust INR methods are presented in Figure 8b and 8c, respectively. Although both methods accomplish reconstruction over the large gaps, our method demonstrates a substantial denoising improvement. Figure 8d shows the errors between the original data and the reconstructed result using the proposed method, explicitly focusing on the existing traces in the original data to highlight the successful reconstruction of valuable signals with only residual noise remaining.

Moving to Figure 9a, we show the data for CMPx numbers 1, 3, 5, and 7 at the same offset and azimuth bin. Subsequently, Figure 9b and 9c shows the reconstructed outcomes by the POCS and robust INR methods, respectively. Our method outperforms POCS, particularly in reconstructing clean and continuous events more effectively. Furthermore, Figure 9d presents the errors between the original data and the reconstructed result using our proposed method. The absence of signal differences, with only the noise being revealed, suggests that our method successfully recovers potential events, maintaining the same structure as POCS.

When we compare synthetic and real data examples, we conclude that our robust INR method demonstrates efficacy in handling 5D seismic data with regular binning. To summarize, when contrasted with the POCS method, our approach not only successfully captures all the events that POCS captured but also effectively attenuates a significant amount of noise, as indicated by Figures 8d and 9d. Furthermore, the events our proposed method captures exhibit more consistent amplitudes, highlighting another advantage of our approach in enhancing the quality of 5D seismic data reconstruction.

#### Real 5D example on an irregular grid

In this example, we apply our proposed method to reconstruct real 5D seismic data directly using the original irregular coordinates. The acquisition

geometry of the survey is shown in Figure 10, where the sources are represented in red and the receivers in blue. The data set includes 446,487 traces. We compute the four spatial coordinates (CMPx, CMPy, offset, and azimuth) for each trace based on the source and receiver coordinates using the following equations:

$$\begin{aligned} \text{CMPx} &= \frac{Sx + Rx}{2} \\ \text{CMPy} &= \frac{Sy + Ry}{2} \\ hx &= Sx - Rx \\ hy &= Sy - Ry \\ h &= \sqrt{hx^2 + hy^2} \\ az &= \frac{180}{\pi} \cdot \text{atan2}(hx, hy). \end{aligned} \quad (6)$$

Here,  $(Sx, Sy)$  and  $(Rx, Ry)$  denote the coordinates of the source and receivers, respectively,  $h$  represents the offset, and  $az$  is the azimuth. For this example, we apply a robust INR directly to the data

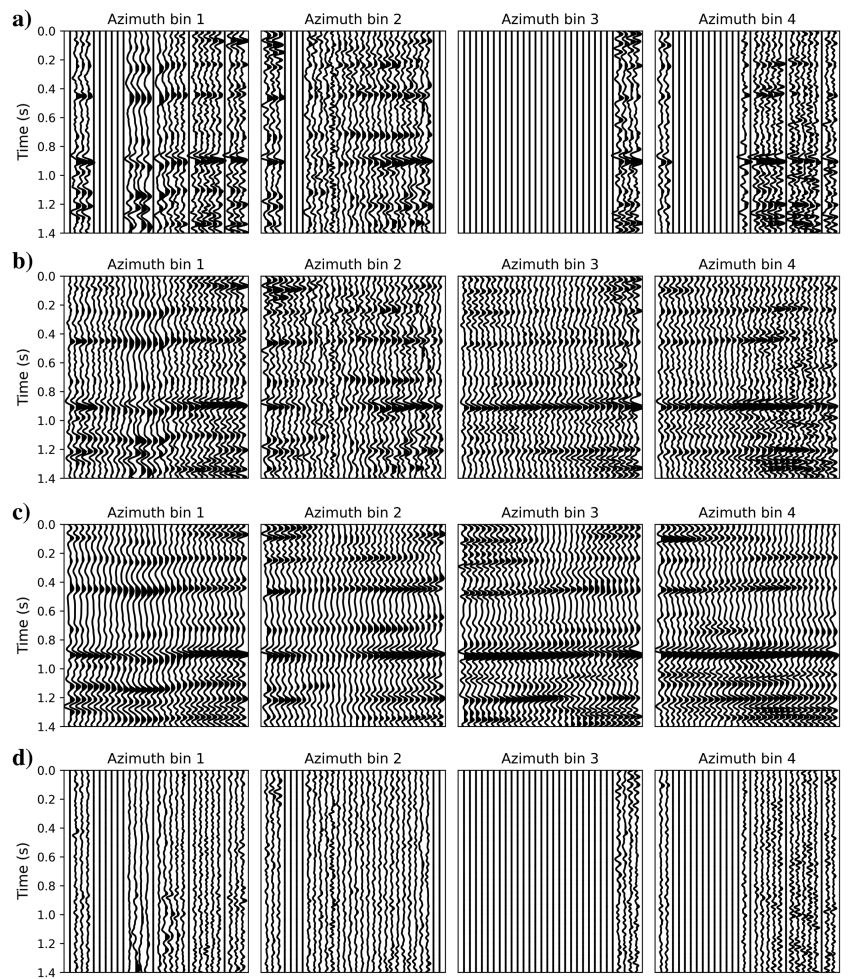


Figure 8. Binned 5D field data example with fixed offset and CMPy. (a) The original data, (b) POCS reconstruction, (c) robust INR reconstruction, and (d) the difference between (a and c).

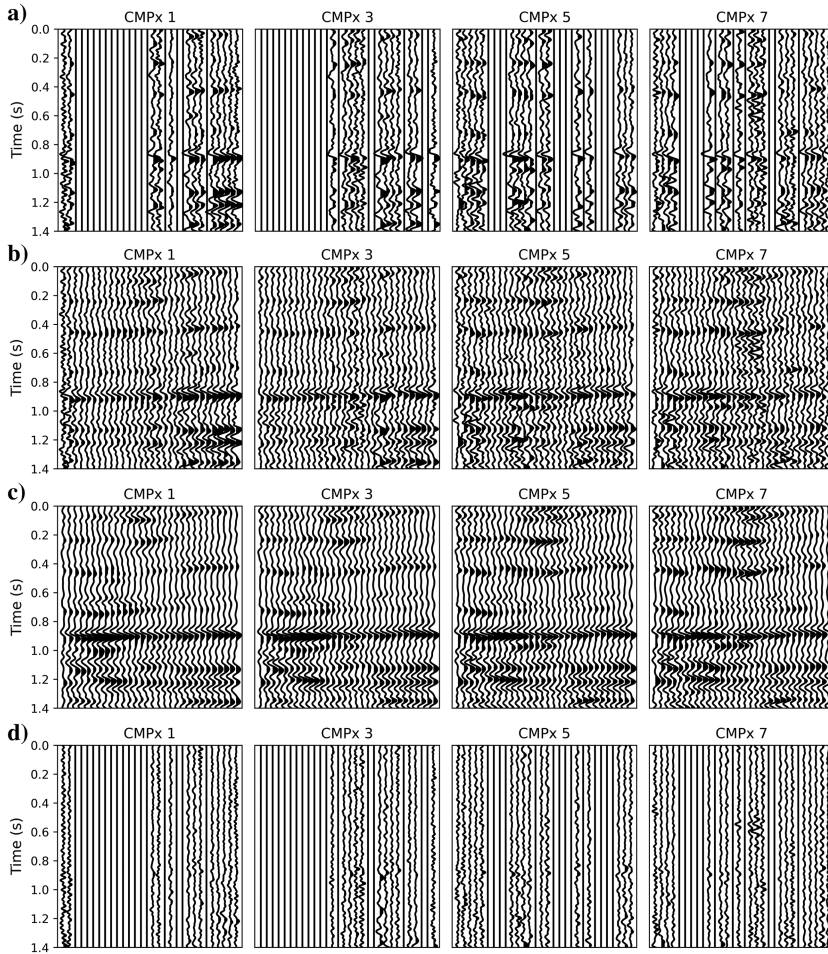


Figure 9. Binned 5D field data example with fixed offset and Azimuth. (a) The original data, (b) POCS reconstruction, (c) robust INR reconstruction, and (d) the difference between (a and c).

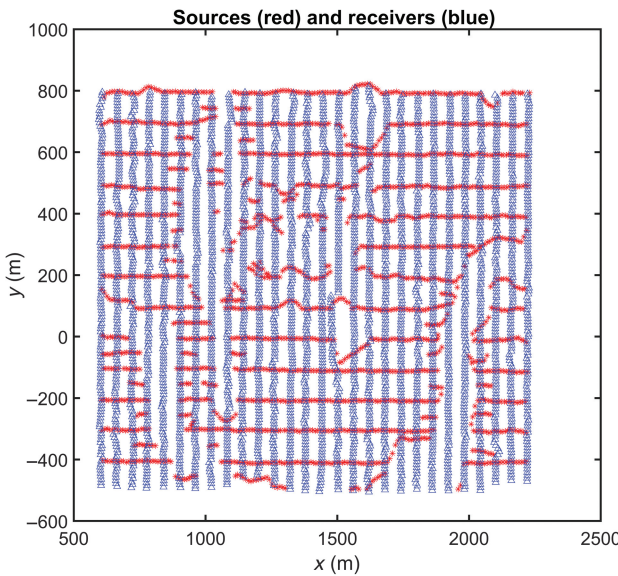


Figure 10. Survey acquisition geometry. The sources are plotted in red, and the receivers are plotted in blue.

with irregular spatial coordinates and then use the trained model to predict the data on regularly binned coordinates. For regular binning, we defined the following geometry:

- $\Delta x = 50$  m, with 20 midpoints in the inline direction.
- $\Delta y = 50$  m, with 280 midpoints in the crossline direction.
- $\Delta h = 1000$  m, resulting in a total of 13 offset sectors.
- $\Delta\phi = 45^\circ$ , leading to a total of eight azimuth sectors.

Figure 11 shows the results of the CMPx section with a fixed offset but varying azimuth degrees. For better visualization, the stacked result for this CMPx section is also shown in Figure 12, where the data are stacked along all offset and azimuth dimensions. The stacked section for the original binned data set contains no missing traces, making it an ideal reference for comparing the interpolated data with the original. In the binned section, we can observe that the weak signals are clearer and more continuous (as indicated by the red rectangles) in the INR results. Furthermore, the average frequency spectrum for the stacked CMPx section is presented in Figure 13. From the average spectrum, it is evident that both methods of interpolation yield peak frequencies at the exact locations of the original data, indicating the accuracy of the interpolated results.

## DISCUSSION

### Optimal $\omega_0$ , loss function, and early stopping criteria

As mentioned previously, to enhance the robustness of our method toward undersampled data with noise, it's crucial to carefully select an optimal value for  $\omega_0$ , use a robust loss function, and determine the appropriate early stopping point. We will investigate the specifics of these selections in the following explanation. Figure 14a and 14b shows the S/N of the reconstructed result for the examples in Figure 3b with varying values of  $\omega_0$  and loss functions, respectively. Figure 14c shows the change of the loss energy (normalized for better comparison) with different loss functions. In Figure 14a, we observe that a larger value of  $\omega_0$  facilitates faster network convergence with  $\ell_2$  norm loss function, reaching the peak S/N value in fewer epochs. However, this increase in  $\omega_0$  may also result in the inadvertent learning of noise, potentially reducing the peak S/N value. When  $\omega_0$  is too small (e.g., 5 rad/s), the network fails to reconstruct the desired signal. For this example, using  $\omega_0$  values between 7–15 rad/s yields the best results. The network rapidly assimilates the signal during the initial stages and then slowly begins to integrate the noise as the training progresses. However, it does not thoroughly learn all the noise in the original noisy data when converging. These observations align with the characteristics of the network mentioned previously.

Analysis of Figure 14b reveals that incorporating a Huber loss function (a smoothed  $\ell_1$  loss) can significantly enhance denoising performance on a noisy data set but with a trade-off of slower convergence rates. In contrast, the  $\ell_1$  norm loss function may not yield as high a peak S/N as the Huber loss function and also has the slowest convergence rate among the three considered. Notably, the  $\ell_1$  norm loss function demonstrates remarkable robustness against erratic noise, characterized by the slowest decline in S/N postpeak attainment.

Figure 14c shows the loss evolution across the epochs for each loss function. This visualization effectively illustrates a distinct turning point in the loss reduction rate for each function. Specifically, the turning points occur approximately at 900 epochs for the  $\ell_2$  norm loss function, 2200 epochs for the Huber loss function, and 3100 epochs for the  $\ell_1$  norm loss function. Remarkably, these turning points align precisely with the

respective peak S/N values for each loss function, indicating a practical criterion for early termination based on loss function behavior.

In conclusion, when dealing with noisy data sets exhibiting a clear turning point in the loss function graph, using the Huber loss function

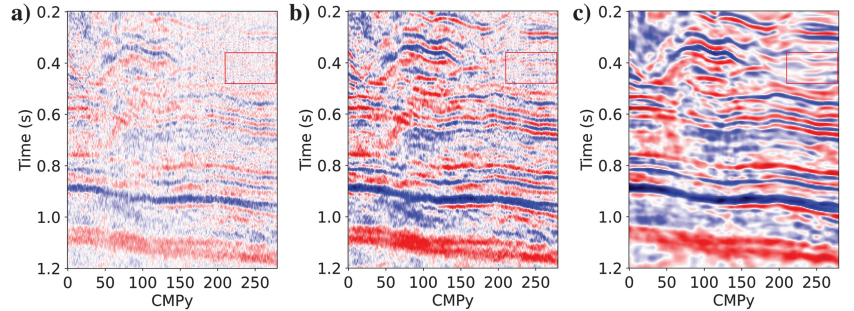


Figure 12. Stacked CMPx section of the reconstructed field data. (a) The original data, (b) POCS, and (c) robust INR with the original irregular coordinates.

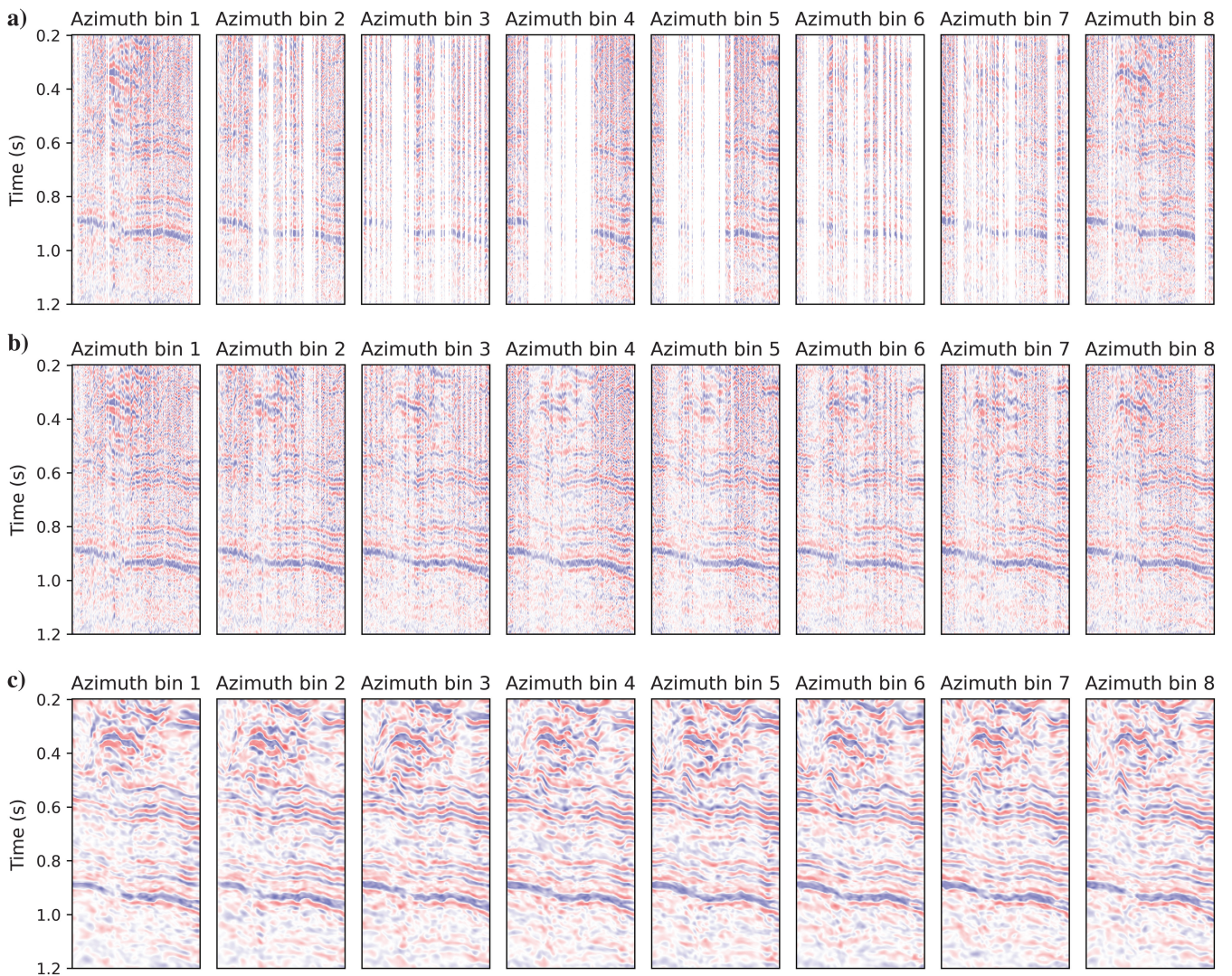


Figure 11. The CMPx section of the reconstructed field seismic data with a fixed offset but different azimuth sectors. (a) The original data, (b) POCS, and (c) robust INR with the original irregular coordinates.

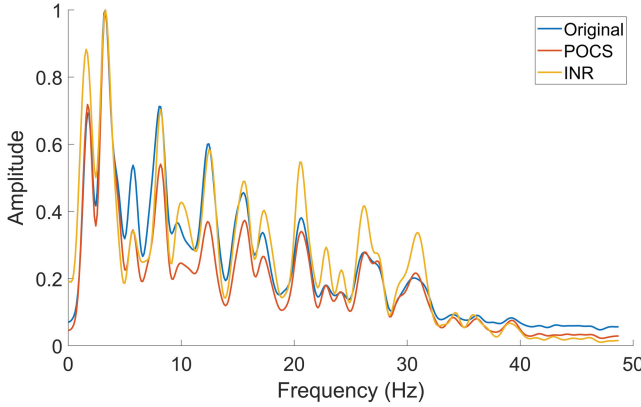


Figure 13. Average frequency spectrum for the stacked CMPx section.

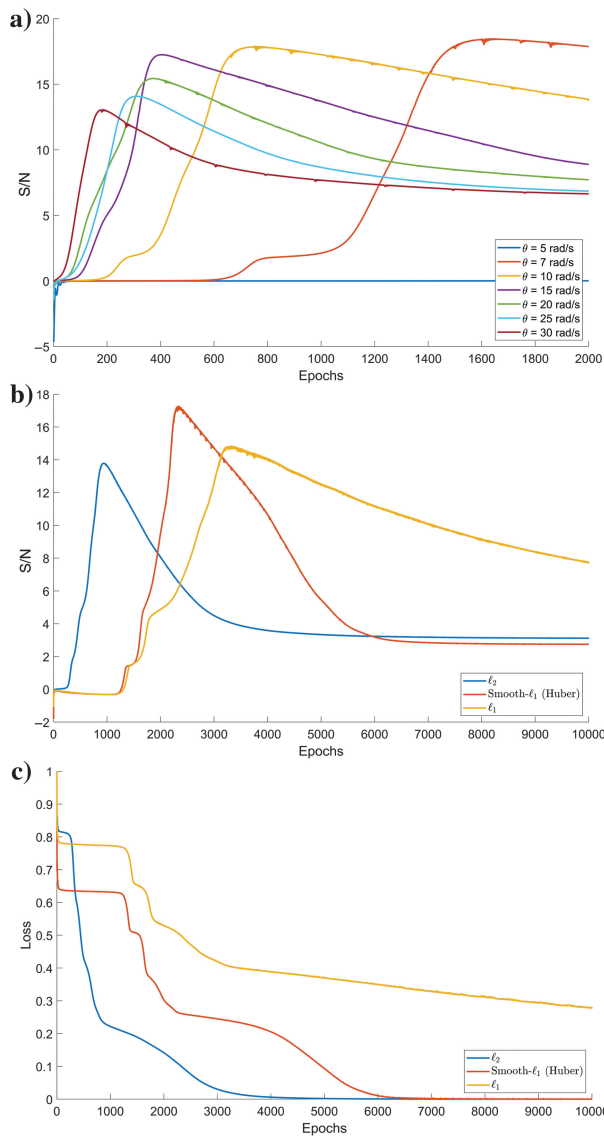


Figure 14. The proposed methods' behavior with different  $\omega_0$  and loss functions. (a) S/N with different  $\omega_0$ , (b) S/N with different loss functions, and (c) the change of loss value with different loss functions.

is advisable for interpolating seismic data. However, in scenarios wherein the turning point is unclear, such as with real-world data characterized by indistinct signal-to-noise differentiation, opting for the  $\ell_1$  norm loss function with extended training epochs proves more effective for reconstructing incomplete noisy data.

#### Optimal $\omega_0$ with various missing data ratios and noise levels

The optimal value of  $\omega_0$  also varies with different data sets, predominantly influenced by the noise level and the percentage of missing data. As shown in Figure 15a, depicting the peak S/N change for the data set shown in Figure 14 across various missing data rates, it's evident that the optimal  $\omega_0$  decreases as more traces are removed. This trend aligns with findings in Li et al. (2023), suggesting that sparser sampling necessitates smoother fitting, which logically demands a smaller  $\omega_0$ . Specifically, our method exhibits robustness even when 80% of the traces are absent, as shown in Figure 16, where the interpolated result using only 20% irregularly sampled traces is presented.

Figure 15b shows the variation in the peak S/N for an input data set across different noise levels. In this scenario, we aim to assess how the optimal value of  $\omega_0$  changes with varying noise levels. Hence, we use fully sampled data to evaluate the denoising efficacy of the proposed method. Across data sets with differing noise levels, using a smaller  $\omega_0$  consistently yields more robust results against the noise in the reconstructed data. In this instance, using  $\omega_0 = 5$  rad/s consistently yields optimal denoising performance. Figure 17 presents the

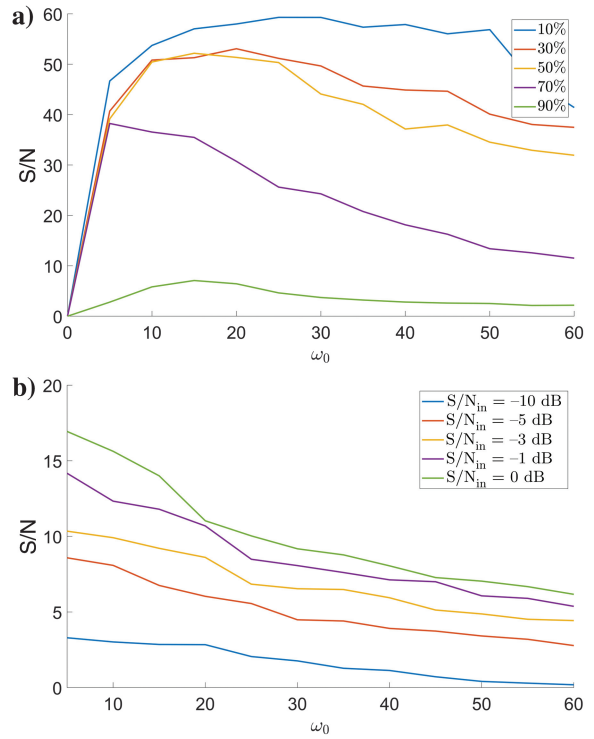


Figure 15. Optimal  $\omega_0$  for data with different percentages of missing traces and different noise levels. (a) The peak S/N for data with different percentages of missing traces, and (b) the peak S/N for input data with different noise levels.

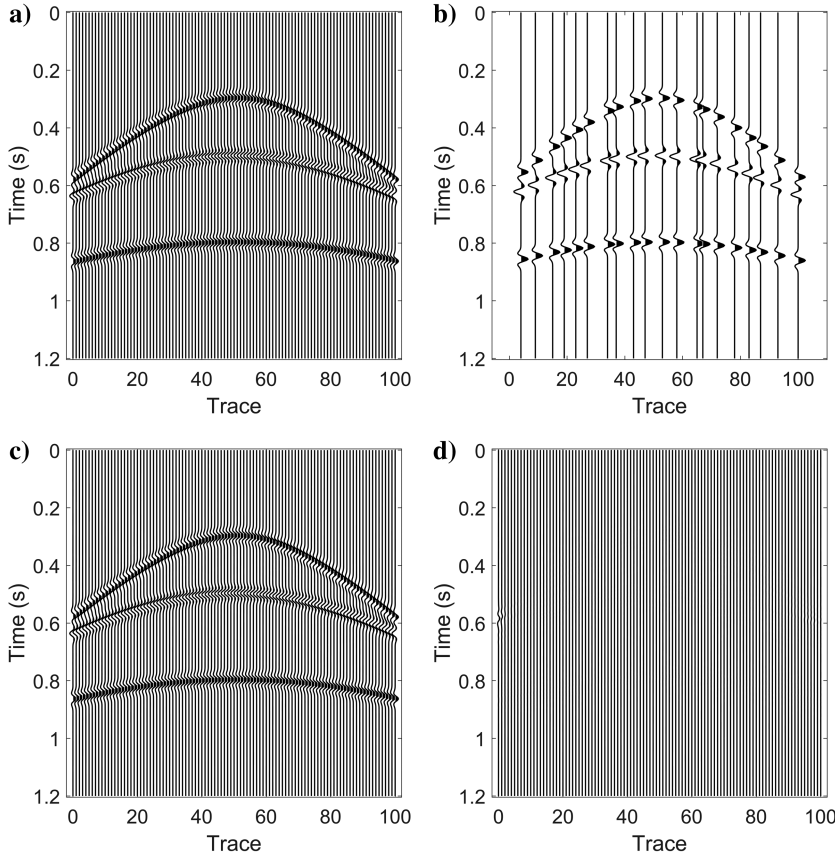


Figure 16. The 2D synthetic example on an irregular grid. (a) The original regularly sampled data, (b) undersampled data with only 20% of the irregularly sampled traces, (c) reconstructed result on the same regular grid as (a) ( $S/N = 30.83$  dB), and (d) errors between (a and c).

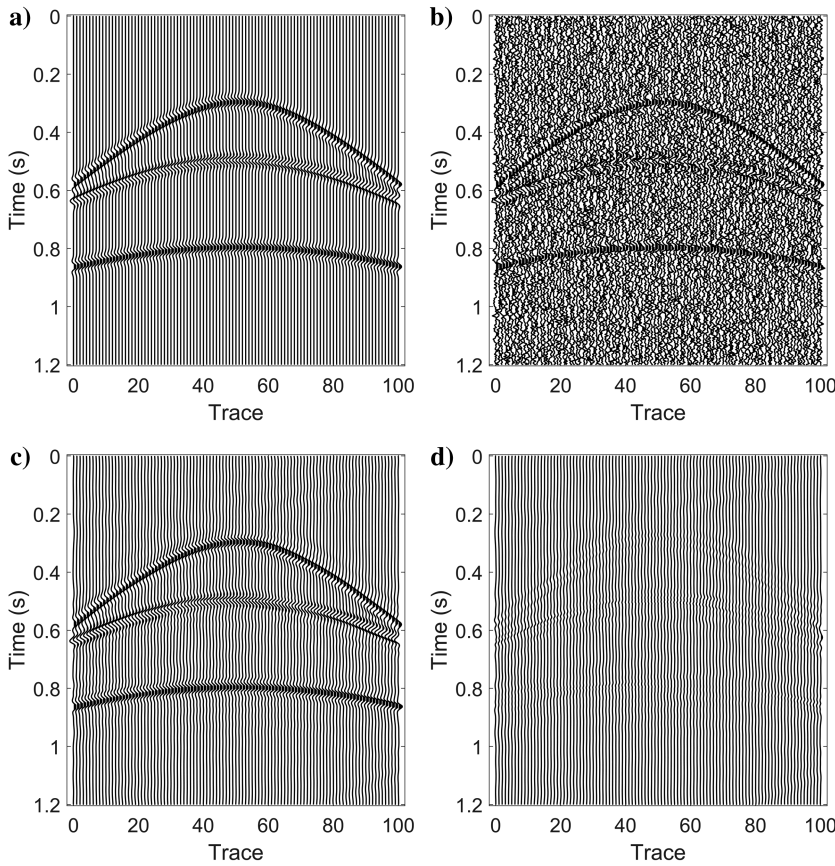


Figure 17. The 2D synthetic example with noise. (a) The original fully sampled data, (b) noisy fully sampled data with the input  $S/N$  equal to  $-5$  dB, (c) denoised result ( $S/N = 9.3$  dB), and (d) errors between (a and c).

denoising performance of our method for noisy data with an input S/N of  $-5$  dB. Although the method may falter in achieving satisfactory denoising outcomes under extremely high noise levels (such as  $-10$  dB), it consistently yields commendable results across various scenarios. Notably, the denoising efficacy primarily hinges on the inherent properties of the network itself. We suggest that integrating additional strategies, such as incorporating a regularization term, holds promise in further enhancing the denoising capabilities of our method.

Hence, achieving the optimal  $\omega_0$  requires considering the input data's missing rate and noise level; for instance, setting  $\omega_0 = 5$  rad/s results in optimal denoising performance when dealing with fully sampled data. However, as depicted in Figure 14a, when the data set contains noise and missing traces, using  $\omega_0 = 5$  rad/s fails to reconstruct the data adequately.

### Limitation in the 5D case

For the 5D examples, we recognize that traditional signal processing methods similar to POCS yield results that better preserve the data's characteristics compared with our proposed method. In other words, the proposed technique tends to produce overly smooth results. This phenomenon is similar to the CRS-based imaging and reconstruction (Baykulov and Gajewski, 2009; Hoecht et al., 2009), wherein results can appear excessively smooth, giving the impression of being numerically generated. Our proposed method encounters a similar issue, which is not uncommon. Several articles have indicated the difficulty of neural networks in modeling high-frequency data. However, as demonstrated in the previous 2D Marmousi example, by using the larger  $\omega_0$ , the network can learn the high-frequency components as well. We believe that similar outcomes can be achieved with 5D data through more careful parameter tuning, especially concerning the learning rate, and by increasing the number of learning epochs. However, achieving this is challenging with our current GPU resources. This characteristic does not invalidate our results; in contrast, it motivates us to pursue further research aimed at developing networks capable of competing with established and robust reconstruction methods based on signal processing in terms of speed and accuracy.

### CONCLUSION

We present an unsupervised framework for interpolating 5D seismic data across regular and irregular grids. Our framework leverages an INR network comprising an MLP with linear layers and element-wise sinusoidal activation functions. Three different loss functions are discussed to enhance the reconstruction of seismic data. By using a small value for  $\omega_0$  and implementing an early stopping criterion, our method not only interpolates 5D seismic data but also effectively suppresses random and erratic noise during the training phase. Comprehensive evaluations conducted on synthetic and real 5D data examples validate the robustness and accuracy of our approach. Specifically, when we adopt binned data, our proposed method yields results comparable to those achieved by POCS but with significantly reduced noise levels. Moreover, using the original irregular spatial coordinates in our approach enables the recovery of faint events that may have been distorted during the binning process, further highlighting the adaptability and superior performance in capturing the details of seismic wavefields.

### ACKNOWLEDGMENTS

We thank the sponsors of CREWES for their continued support. This work is funded by the CREWES industrial sponsors and the Natural Science and Engineering Research Council of Canada (NSERC) through grant CRDPJ 543578-19. The contribution of the second author is supported by the industrial sponsors of the Signal Analysis and Imaging Group (SAIG) consortium at the University of Alberta.

### DATA AND MATERIALS AVAILABILITY

Data associated with this research are available and can be obtained by contacting the corresponding author.

### REFERENCES

- Abma, R., and N. Kabir, 2006, 3D interpolation of irregular data with a POCS algorithm: *Geophysics*, **71**, no. 6, E91–E97, doi: [10.1190/1.2356088](https://doi.org/10.1190/1.2356088).
- Bardan, V., 1987, Trace interpolation in seismic data processing: *Geophysical Prospecting*, **35**, 343–358, doi: [10.1111/j.1365-2478.1987.tb00822.x](https://doi.org/10.1111/j.1365-2478.1987.tb00822.x).
- Barron, J. T., B. Mildenhall, M. Tancik, P. Hedman, R. Martin-Brualla, and P. P. Srinivasan, 2021, Mip-NeRF: A multiscale representation for anti-aliasing neural radiance fields: *Proceedings of the IEEE/CVF International Conference on Computer Vision*, 5855–5864.
- Baykulov, M., and D. Gajewski, 2009, Prestack seismic data enhancement with partial common-reflection-surface (CRS) stack: *Geophysics*, **74**, no. 3, V49–V58, doi: [10.1190/1.3106182](https://doi.org/10.1190/1.3106182).
- Carozzi, F., and M. D. Sacchi, 2019, Robust tensor-completion algorithm for 5D seismic-data reconstruction: *Geophysics*, **84**, no. 2, V97–V109, doi: [10.1190/geo2018-0109.1](https://doi.org/10.1190/geo2018-0109.1).
- Cavalcante, Q., and M. J. Porsani, 2022, Low-rank seismic data reconstruction and denoising by CUR matrix decompositions: *Geophysical Prospecting*, **70**, 362–376, doi: [10.1111/1365-2478.13163](https://doi.org/10.1111/1365-2478.13163).
- Chan, E. R., M. Monteiro, P. Kellnhofer, J. Wu, and G. Wetzstein, 2021, pi-GAN: Periodic implicit generative adversarial networks for 3D-aware image synthesis: *Proceedings of the IEEE/CVF conference on computer vision and pattern recognition*, 5799–5809.
- Chen, Y., D. Zhang, Z. Jin, X. Chen, S. Zu, W. Huang, and S. Gan, 2016, Simultaneous denoising and reconstruction of 5-D seismic data via damped rank-reduction method: *Geophysical Journal International*, **206**, 1695–1717, doi: [10.1093/gji/ggw230](https://doi.org/10.1093/gji/ggw230).
- Chiu, S. K., 2014, Multidimensional interpolation using a model-constrained minimum weighted norm interpolation: *Geophysics*, **79**, no. 5, V191–V199, doi: [10.1190/geo2014-0086.1](https://doi.org/10.1190/geo2014-0086.1).
- Duijndam, A., and M. Schoneville, 1999, Nonuniform fast Fourier transform: *Geophysics*, **64**, 539–551, doi: [10.1190/1.1444560](https://doi.org/10.1190/1.1444560).
- Duijndam, A., M. Schoneville, and C. Hindriks, 1999, Reconstruction of band-limited signals, irregularly sampled along one spatial direction: *Geophysics*, **64**, 524–538, doi: [10.1190/1.1444559](https://doi.org/10.1190/1.1444559).
- Ely, G., S. Aeron, N. Hao, and M. E. Kilmer, 2013, 5D and 4D pre-stack seismic data completion using tensor nuclear norm (TNN): 83rd Annual International Meeting, SEG, Expanded Abstracts, 3639–3644, doi: [10.1190/segam2013-1143.1](https://doi.org/10.1190/segam2013-1143.1).
- Ely, G., S. Aeron, N. Hao, and M. E. Kilmer, 2015, 5D seismic data completion and denoising using a novel class of tensor decompositions: *Geophysics*, **80**, no. 4, V83–V95, doi: [10.1190/geo2014-0467.1](https://doi.org/10.1190/geo2014-0467.1).
- Gao, J., J. Cheng, and M. D. Sacchi, 2016, Five-dimensional seismic reconstruction using parallel square matrix factorization: *IEEE Transactions on Geoscience and Remote Sensing*, **55**, 2124–2135, doi: [10.1109/TGRS.2016.2636864](https://doi.org/10.1109/TGRS.2016.2636864).
- Gao, J., M. D. Sacchi, and X. Chen, 2013a, A fast reduced-rank interpolation method for prestack seismic volumes that depend on four spatial dimensions: *Geophysics*, **78**, no. 1, V21–V30, doi: [10.1190/geo2012-0038.1](https://doi.org/10.1190/geo2012-0038.1).
- Gao, J., A. Stanton, M. Naghizadeh, M. D. Sacchi, and X. Chen, 2013b, Convergence improvement and noise attenuation considerations for beyond alias projection onto convex sets reconstruction: *Geophysical Prospecting*, **61**, 138–151, doi: [10.1111/j.1365-2478.2012.01103.x](https://doi.org/10.1111/j.1365-2478.2012.01103.x).
- Gao, J., A. Stanton, and M. D. Sacchi, 2015, Parallel matrix factorization algorithm and its application to 5D seismic reconstruction and denoising: *Geophysics*, **80**, no. 6, V173–V187, doi: [10.1190/geo2014-0594.1](https://doi.org/10.1190/geo2014-0594.1).
- Hennenfent, G., L. Fenellos, and F. J. Herrmann, 2010, Nonequispaced curvelet transform for seismic data reconstruction: A sparsity-promoting approach: *Geophysics*, **75**, no. 6, WB203–WB210, doi: [10.1190/1.3494032](https://doi.org/10.1190/1.3494032).

- Herrmann, F. J., and G. Hennenfent, 2008, Non-parametric seismic data recovery with curvelet frames: *Geophysical Journal International*, **173**, 233–248, doi: [10.1111/j.1365-246X.2007.03698.x](https://doi.org/10.1111/j.1365-246X.2007.03698.x).
- Hoecht, G., P. Ricarte, S. Bergler, and E. Landa, 2009, Operator-oriented CRS interpolation: *Geophysical Prospecting*, **57**, 957–979, doi: [10.1111/j.1365-2478.2009.00789.x](https://doi.org/10.1111/j.1365-2478.2009.00789.x).
- Huh, M., H. Mobahi, R. Zhang, B. Cheung, P. Agrawal, and P. Isola, 2021, The low-rank simplicity bias in deep networks: arXiv preprint, doi: [10.48550/arXiv.2103.10427](https://doi.org/10.48550/arXiv.2103.10427).
- Jiang, T., B. Gong, F. Qiao, Y. Jiang, A. Chen, D. Hren, and Z. Meng, 2017, Compressive seismic reconstruction with extended POCS for arbitrary irregular acquisition: 87th Annual International Meeting, SEG, Expanded Abstracts, 4272–4277, doi: [10.1190/segam2017-17632472.1](https://doi.org/10.1190/segam2017-17632472.1).
- Jin, S., 2010, 5D seismic data regularization by a damped least-norm Fourier inversion: *Geophysics*, **75**, no. 6, WB103–WB111, doi: [10.1190/1.3505002](https://doi.org/10.1190/1.3505002).
- Kabir, M. N., and D. Verschuur, 1995, Restoration of missing offsets by parabolic Radon transform: *Geophysical Prospecting*, **43**, 347–368, doi: [10.1111/j.1365-2478.1995.tb00257.x](https://doi.org/10.1111/j.1365-2478.1995.tb00257.x).
- Keiner, J., S. Kunis, and D. Potts, 2009, Using NFFT 3 — A software library for various nonequispaced fast Fourier transforms: *ACM Transactions on Mathematical Software*, **36**, 1–30, doi: [10.1145/1555386.1555388](https://doi.org/10.1145/1555386.1555388).
- Kreimer, N., and M. D. Sacchi, 2012, A tensor higher-order singular value decomposition for prestack seismic data noise reduction and interpolation: *Geophysics*, **77**, no. 3, V113–V122, doi: [10.1190/geo2011-0399.1](https://doi.org/10.1190/geo2011-0399.1).
- Kreimer, N., A. Stanton, and M. D. Sacchi, 2013, Tensor completion based on nuclear norm minimization for 5D seismic data reconstruction: *Geophysics*, **78**, no. 6, V273–V284, doi: [10.1190/geo2013-0022.1](https://doi.org/10.1190/geo2013-0022.1).
- Kumar, R., C. Da Silva, O. Akalin, A. Y. Aravkin, H. Mansour, B. Recht, and F. J. Herrmann, 2015, Efficient matrix completion for seismic data reconstruction: *Geophysics*, **80**, no. 5, V97–V114, doi: [10.1190/geo2014-0369.1](https://doi.org/10.1190/geo2014-0369.1).
- Li, C., C. C. Mosher, and S. T. Kaplan, 2012, Interpolated compressive sensing for seismic data reconstruction: 82nd Annual International Meeting, SEG, Expanded Abstracts, doi: [10.1190/segam2012-1335.1](https://doi.org/10.1190/segam2012-1335.1).
- Li, Z., H. Wang, and D. Meng, 2023, Regularize implicit neural representation by itself: Proceedings of the IEEE/CVF Conference on Computer Vision and Pattern Recognition, 10280–10288.
- Liu, B., and M. D. Sacchi, 2004, Minimum weighted norm interpolation of seismic records: *Geophysics*, **69**, 1560–1568, doi: [10.1190/1.1836829](https://doi.org/10.1190/1.1836829).
- Liu, D., M. D. Sacchi, and W. Chen, 2022, Efficient tensor completion methods for 5D seismic data reconstruction: Low-rank tensor train and tensor ring: *IEEE Transactions on Geoscience and Remote Sensing*, **60**, 1–17, doi: [10.1109/TGRS.2022.3179275](https://doi.org/10.1109/TGRS.2022.3179275).
- Liu, D., W. Gao, W. Xu, J. Li, X. Wang, and W. Chen, 2024, 5-D seismic data interpolation by continuous representation: *IEEE Transactions on Geoscience and Remote Sensing*, **62**, 1–11, doi: [10.1109/TGRS.2024.3431439](https://doi.org/10.1109/TGRS.2024.3431439).
- López, O., R. Kumar, O. Yilmaz, and F. J. Herrmann, 2016, Off-the-grid low-rank matrix recovery and seismic data reconstruction: *IEEE Journal of Selected Topics in Signal Processing*, **10**, 658–671, doi: [10.1109/JSTSP.2016.2555482](https://doi.org/10.1109/JSTSP.2016.2555482).
- Martin-Brualla, R., N. Radwan, M. S. Sajjadi, J. T. Barron, A. Dosovitskiy, and D. Duckworth, 2021, NeRF in the wild: Neural radiance fields for unconstrained photo collections: Proceedings of the IEEE/CVF Conference on Computer Vision and Pattern Recognition, 7210–7219.
- Mildenhall, B., P. P. Srinivasan, M. Tancik, J. T. Barron, R. Ramamoorthi, and R. Ng, 2021, NeRF: Representing scenes as neural radiance fields for view synthesis: *Communications of the ACM*, **65**, 99–106, doi: [10.1145/3503250](https://doi.org/10.1145/3503250).
- Mosher, C. C., C. Li, F. D. Janiszewski, L. S. Williams, T. C. Carey, and Y. Ji, 2017, Operational deployment of compressive sensing systems for seismic data acquisition: *The Leading Edge*, **36**, 661–669, doi: [10.1190/tle36080661.1](https://doi.org/10.1190/tle36080661.1).
- Naghizadeh, M., and M. D. Sacchi, 2009, F-X adaptive seismic-trace interpolation: *Geophysics*, **74**, no. 1, V9–V16, doi: [10.1190/1.3008547](https://doi.org/10.1190/1.3008547).
- Oliveira, D. A., R. S. Ferreira, R. Silva, and E. V. Brazil, 2018, Interpolating seismic data with conditional generative adversarial networks: *IEEE Geoscience and Remote Sensing Letters*, **15**, 1952–1956, doi: [10.1109/LGRS.2018.2866199](https://doi.org/10.1109/LGRS.2018.2866199).
- Oropeza, V., and M. Sacchi, 2011, Simultaneous seismic data denoising and reconstruction via multichannel singular spectrum analysis: *Geophysics*, **76**, no. 3, V25–V32, doi: [10.1190/1.3552706](https://doi.org/10.1190/1.3552706).
- Park, M. J., J. Jennings, B. Clapp, and B. Biondi, 2020, Seismic data interpolation using a POCS-guided deep image prior: 90th Annual International Meeting, SEG, Expanded Abstracts, 3154–3158, doi: [10.1190/segam2020-3427320.1](https://doi.org/10.1190/segam2020-3427320.1).
- Popa, J., S. E. Minkoff, and Y. Lou, 2021, An improved seismic data completion algorithm using low-rank tensor optimization: Cost reduction and optimal data orientation: *Geophysics*, **86**, no. 3, V219–V232, doi: [10.1190/geo2020-0539.1](https://doi.org/10.1190/geo2020-0539.1).
- Porsani, M. J., 1999, Seismic trace interpolation using half-step prediction filters: *Geophysics*, **64**, 1461–1467, doi: [10.1190/1.1444650](https://doi.org/10.1190/1.1444650).
- Qian, F., Z. Liu, Y. Wang, S. Liao, S. Pan, and G. Hu, 2021, DTAE: Deep tensor autoencoder for 3-D seismic data interpolation: *IEEE Transactions on Geoscience and Remote Sensing*, **60**, 1–19, doi: [10.1109/TGRS.2021.3075968](https://doi.org/10.1109/TGRS.2021.3075968).
- Rahaman, N., A. Baratin, D. Arpit, F. Draxler, M. Lin, F. Hamprecht, Y. Bengio, and A. Courville, 2019, On the spectral bias of neural networks: International Conference on Machine Learning, 5301–5310.
- Sacchi, M. D., and T. J. Ulrych, 1995, High-resolution velocity gathers and offset space reconstruction: *Geophysics*, **60**, 1169–1177, doi: [10.1190/1.1443845](https://doi.org/10.1190/1.1443845).
- Sacchi, M. D., and T. J. Ulrych, 1996, Estimation of the discrete fourier transform, a linear inversion approach: *Geophysics*, **61**, 1128–1136, doi: [10.1190/1.1444033](https://doi.org/10.1190/1.1444033).
- Sacchi, M. D., T. J. Ulrych, and C. J. Walker, 1998, Interpolation and extrapolation using a high-resolution discrete Fourier transform: *IEEE Transactions on Signal Processing*, **46**, 31–38, doi: [10.1109/78.651165](https://doi.org/10.1109/78.651165).
- Sitzmann, V., J. Martel, A. Bergman, D. Lindell, and G. Wetzstein, 2020, Implicit neural representations with periodic activation functions: Advances in Neural Information Processing Systems, 7462–7473.
- Spitz, S., 1991, Seismic trace interpolation in the FX domain: *Geophysics*, **56**, 785–794, doi: [10.1190/1.1443096](https://doi.org/10.1190/1.1443096).
- Sternfels, R., G. Viguer, R. Gondoin, and D. Le Meur, 2015, Multidimensional simultaneous random plus erratic noise attenuation and interpolation for seismic data by joint low-rank and sparse inversion: *Geophysics*, **80**, no. 6, WD129–WD141, doi: [10.1190/geo2015-0066.1](https://doi.org/10.1190/geo2015-0066.1).
- Tancik, M., P. Srinivasan, B. Mildenhall, S. Fridovich-Keil, N. Raghavan, U. Singhal, R. Ramamoorthi, J. Barron, and R. Ng, 2020, Fourier features let networks learn high frequency functions in low dimensional domains: Advances in Neural Information Processing Systems, 7537–7547.
- Tošić, I., and P. Frossard, 2011, Dictionary learning: *IEEE Signal Processing Magazine*, **28**, 27–38.
- Trad, D., 2009, Five-dimensional interpolation: Recovering from acquisition constraints: *Geophysics*, **74**, no. 6, V123–V132, doi: [10.1190/1.3245216](https://doi.org/10.1190/1.3245216).
- Trickett, S., L. Burroughs, A. Milton, L. Walton, and R. Dakic, 2010, Rank-reduction-based trace interpolation: 80th Annual International Meeting, SEG, Expanded Abstracts, 3829–3833, doi: [10.1190/1.3513645](https://doi.org/10.1190/1.3513645).
- Wang, B., N. Zhang, W. Lu, and J. Wang, 2019, Deep-learning-based seismic data interpolation: A preliminary result: *Geophysics*, **84**, no. 1, V11–V20, doi: [10.1190/geo2017-0495.1](https://doi.org/10.1190/geo2017-0495.1).
- Wang, H., Y. Chen, Y. A. S. I. Oboué, R. Abma, Z. Geng, S. Fomel, and Y. Chen, 2021, Simultaneous reconstruction and denoising of extremely sparse 5-D seismic data by a simple and effective method: *IEEE Transactions on Geoscience and Remote Sensing*, **60**, 1–12, doi: [10.1109/TGRS.2021.3132257](https://doi.org/10.1109/TGRS.2021.3132257).
- Wang, J., M. Ng, and M. Perz, 2010, Seismic data interpolation by greedy local Radon transform: *Geophysics*, **75**, no. 6, WB225–WB234, doi: [10.1190/1.3484195](https://doi.org/10.1190/1.3484195).
- Wang, Z., and Y. Li, 1994, Trace interpolation using wavelet transform: 64th Annual International Meeting, SEG, Expanded Abstracts, 729–730, doi: [10.1190/1.1931974](https://doi.org/10.1190/1.1931974).
- Xie, Y., and D. Gajewski, 2016, Interpolation and regularization with the 3D CRS operator: 86th Annual International Meeting, SEG, Expanded Abstracts, 4092–4096, doi: [10.1190/segam2016-1386859.1](https://doi.org/10.1190/segam2016-1386859.1).
- Xie, Y., and D. Gajewski, 2017, 5-D interpolation with wave-front attributes: *Geophysical Journal International*, **211**, 897–919, doi: [10.1093/gji/gjx334](https://doi.org/10.1093/gji/gjx334).
- Xu, S., Y. Zhang, D. Pham, and G. Lambaré, 2005, Antileakage Fourier transform for seismic data regularization: *Geophysics*, **70**, no. 4, V87–V95, doi: [10.1190/1.1993713](https://doi.org/10.1190/1.1993713).
- Xu, W., and J. Jiao, 2023, Revisiting implicit neural representations in low-level vision: arXiv preprint, doi: [10.48550/arXiv.2304.10250](https://doi.org/10.48550/arXiv.2304.10250).
- Xu, Z.-Q. J., 2020, Frequency principle: Fourier analysis sheds light on deep neural networks: *Communications in Computational Physics*, **28**, 1746–1767, doi: [10.4208/cicp.OA-2020-0085](https://doi.org/10.4208/cicp.OA-2020-0085).
- Yuan, P., S. Wang, W. Hu, P. Nadukandi, G. Ocampo Botero, X. Wu, J. Chen, and H. Van Nguyen, 2021, Self-supervised learning for anti-aliasing seismic data interpolation: First International Meeting for Applied Geoscience & Energy, SEG, Expanded Abstracts, 1500–1504, doi: [10.1190/segam2021-3584206.1](https://doi.org/10.1190/segam2021-3584206.1).
- Yuce, G., G. Ortiz-Jimenez, B. Besbinar, and P. Frossard, 2022, A structured dictionary perspective on implicit neural representations: Proceedings of the IEEE/CVF Conference on Computer Vision and Pattern Recognition, 19228–19238.
- Zwartjes, P., and A. Gisolf, 2007, Fourier reconstruction with sparse inversion: *Geophysical Prospecting*, **55**, 199–221, doi: [10.1111/j.1365-2478.2006.00580.x](https://doi.org/10.1111/j.1365-2478.2006.00580.x).

Biographies and photographs of the authors are not available.